termines the local orientation of the discontinuous fibers and therefore the mechanical performance of the part. Molding duration depends on part thickness. After demolding, the part is deburred by milling (f). During milling, the abrupt change of material properties in the interfacial area between CoFRP and DiCoFRP requires tailored machining strategies. Otherwise, pull-out of fibers or local cracks can occur. This may harm the structural integrity of the part and must be avoided.
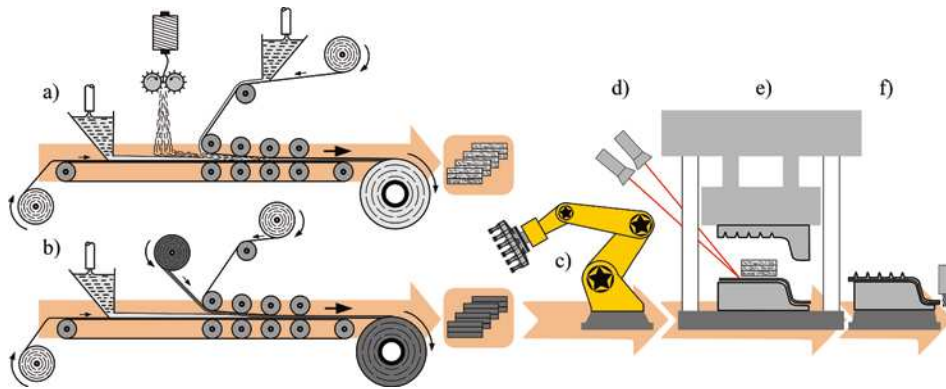
Figure 2.2 CoDiCo structures' manufacturing route [1]

■ 2.2 Processing of CoDiCo Material

David Bücheler

2.2.1 Introduction

Chopped glass and carbon fiber reinforced plastics offer excellent characteristics for complex part geometry, function integration, material utilization, productivity, and economical production. However, limited fiber length and insufficient process control over fiber orientation lead to limited mechanical strength and stiffness.

Continuously fiber reinforced materials, in contrast, exhibit the opposite behavior. That is, they offer superior mechanical properties, but with limited design freedom and high costs.

Co-molding a continuously reinforced material (CoFRP) with a discontinuously reinforced material (DiCoFRP) permits the rapid and cost-effective manufacturing of complex structural composites (CoDiCoFRP). The flowability of DiCoFRP is used to

form complex geometries such as ribs and to integrate inserts, whereas the position and alignment of the continuous fiber material determines the structural integrity of the component.

The research presented in the following subsections is a summary from the doctoral thesis *Locally Continuous-fiber Reinforced Sheet Molding Compound* [2].

Current State of the Science

State of the art, continuously fiber reinforced thermoset material CoFRTS resin systems are based on unsaturated polyester (UP), vinyl ester (VE), or epoxy (EP) matrices. All these resins lack the ability to create a chemically stable, highly viscous B-stage. The viscosity of UP and VE CoFRTS thickened with alkaline earth metal oxides or hydroxides drops dramatically when molded under process conditions at 150 °C. Thus, the CoFRTS cannot withstand the forces applied by the flowing, co-molding material. This behavior is illustrated in Figure 2.3 and also reported in the literature [3, 4]. The B-staging of EP resins leads to higher viscosity levels under compression molding conditions, but the material shows a narrow process window for preforming and a short shelf life [5, 6]. For state-of-the-art resin systems, it is clear that a reinforcing effect can only be achieved by eliminating flow inside the mold. Because DiCoFRP (especially sheet molding compound (SMC)) is known for its superior design freedom and suitability for function integration, this limitation is not acceptable. Thus, material and process development is needed to fix the continuous fiber position and alignment while co-molding.
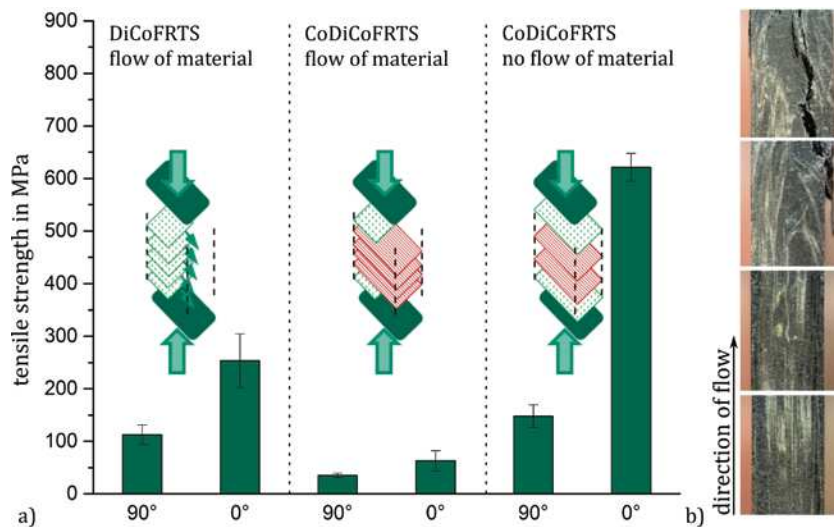
Figure 2.3 (a) Tensile strength as a function of layup and flow. (b) Crack path of CoDiCoFRTS 0° type 2 specimen after flow [2]

Process Chain

The process chain developed here is schematically shown in Figure 2.4. The semi-finished DiCo material (chopped glass or carbon fiber SMC) is produced with the help of a state-of-the-art flat conveyor plant (1a), matured, cut, and combined into a stack (1b). The Co material is manufactured accordingly on a modified and heat-able flat conveyer plant (2a). The Co matrix is based on an unsaturated polyester–polyurethane hybrid resin (UPPH) and is combined with a 50 k carbon fiber non-crimp fabric (NCF). The UPPH resin offers an alternative thickening technology that leads to a stable, highly viscous B-stage. This B-stage is reached in less than five minutes at 80 °C. Thus, the material is viscous enough to enable direct cutting to dimensions of the final reinforcements (2b) without requiring maturation. The Co matrix also contains ferri-magnetic particles, which permits draping of the re-inforcement by one solid mold-half (2c). After a second heating step on the draping device (2d), stiff, B-stage reinforcements (2e) are obtained, which can be stored or processed further. The final part (4) is generated by compression molding (3). Here, magnetic fields are used to fix the local reinforcements inside the mold during co-molding with DiCo material.
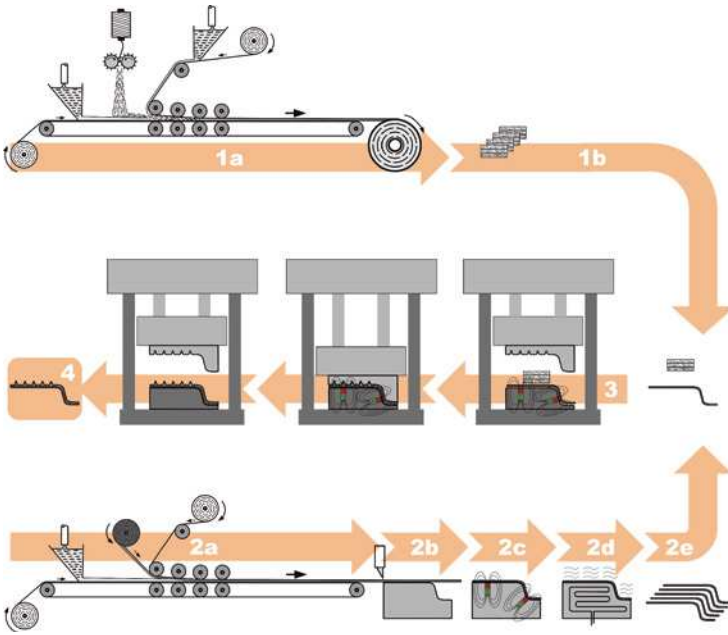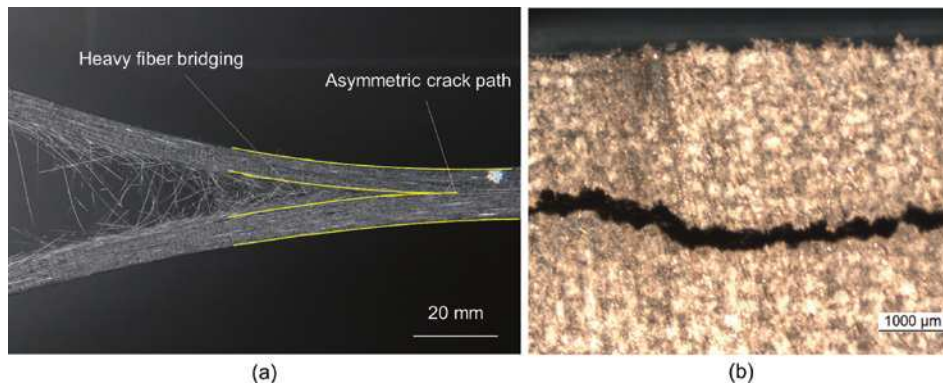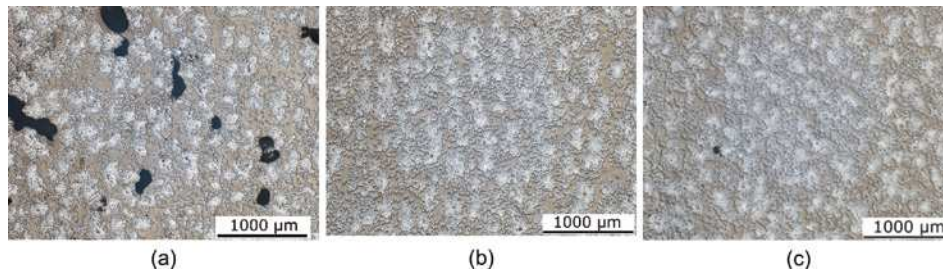

Figure 2.4 Processing CoDiCo material [2]

Figure 3.7 (a) Fracture behavior: extensive fiber-bridging and asymmetric crack propagation and (b) non-planar crack path in the specimen's cross section

3.2.4 Analysis of the Microstructure and Crack-Initiating Factors


Figure 3.8 Micrographs illustrating the microstructure of the plaques with parameter pairings (a) 260-24, (b) 280-36, and (c) 280-48

Micrographs of the consolidated plaques are captured in order to analyze the material's microstructure with respect to the process parameters. An exemplary micrograph of the parameter pairing 260-24 is shown in Figure 3.8(a), 280-36 in Figure 3.8(b), and 280-48 in Figure 3.8(c), respectively. In all three micrographs, the tapes' stacking sequence is from left to right. The plaque's microstructure resulting from the lowest consolidation pressure and lowest temperature, 260-24, is perforated by numerous voids, some of which extend for more than 1 mm. Both the sizes and the positions of the voids are distributed over the entire material. The fibers are primarily arranged in tightly packed bundles with matrix-rich areas surrounding the bundles. A long-range ordering of the bundles indicating the tape layers is slightly visible in the 260-24 micrograph, and also in the 280-36 micro-

graph. Here, the fiber bundles are slightly smaller, but are just as densely packed as those in the 260-24 pairing. On the 280-36 and the 280-48 micrographs, only a few voids with small dimensions are present. The fiber bundles in 280-48 seem to be dispersed more homogenously regarding both their size and their location; no long-range bundle ordering can be identified here. Although the micrographs show that the consolidation process distinctively affects the microstructure, no clear effect on the scattering fracture toughness values is observed. Indeed, size and dispersion of voids might explain why the lowest consolidation pressure results in the highest scatter. However, the specimens that are almost free of voids do not tend to significantly lower scatter in terms of their measured fracture toughness. Thus, the reasons for this phenomenon cannot be identified exclusively by the micrographs.

Compared to an analysis of the general microstructure of consolidated plaques, much more in-depth information about the fracture procedure can be obtained by analyzing the fracture surfaces. For this reason, scanning electron microscopy (SEM) is used for further analyzing the micromechanical fracture processes. As already indicated by the transverse crack path, the fracture surface has a very rough overall topology. The topographical course seems to be driven by ruptures of single fibers but also of entire fiber bundles. This supports the hypothesis made earlier, that failing fiber bridges dissipate fracture energy (which cannot be related to the visually measured crack growth) and hence falsify the computed fracture toughness value. Moreover, the failing fibers rupture into several pieces, which can be found in the surrounding areas of broken fiber ends. Indeed, open voids are visible in specimens made with low consolidation pressure, which corroborates the assumption that the presence of voids increases the scatter in the fracture toughness. However, the pictures also show that voids with rather small cross-sectional areas can be up to several millimeters long. Void analysis by transverse micrographs can therefore be misleading and might underestimate the voids' influence on the mechanical properties of the material.

(a)   (b)
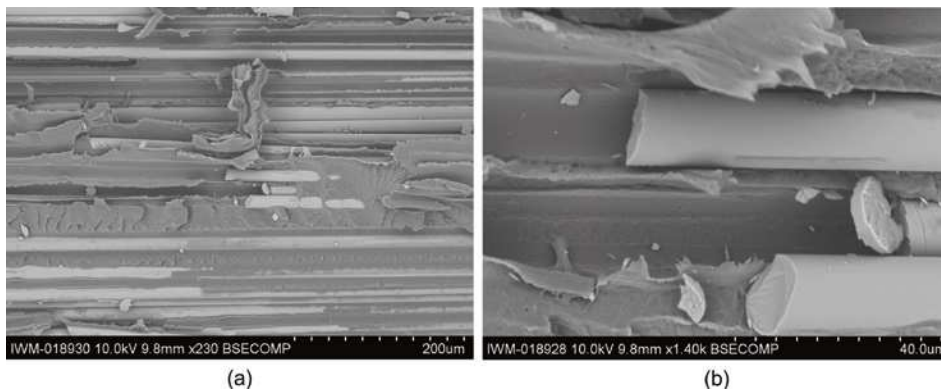
Figure 3.9 SEM micrographs of the fracture surfaces revealing neat fiber surfaces indicating fiber–matrix interface failure

Figure 3.9 shows a SEM micrograph of the analyzed area of the fracture surface and a close-up of broken fibers within the same area. These pictures reveal the remarkable fact that the surfaces of the present glass fibers are almost entirely exposed and that there are smooth cavities formerly filled by ruptured fibers. Between the fibers or fiber cavities, matrix-rich areas are visible in which the polymer is highly plastically deformed and ruptured, partially showing a ductile failure mode. A comparison of the fibers' fracture surfaces in the close-up picture with the fibers' lateral surfaces shows that the neat glass fibers are almost completely exposed with little to no polymer residue on them. This makes it possible to assume that the main fracture driving factor is the failure of the fiber–matrix interfaces.
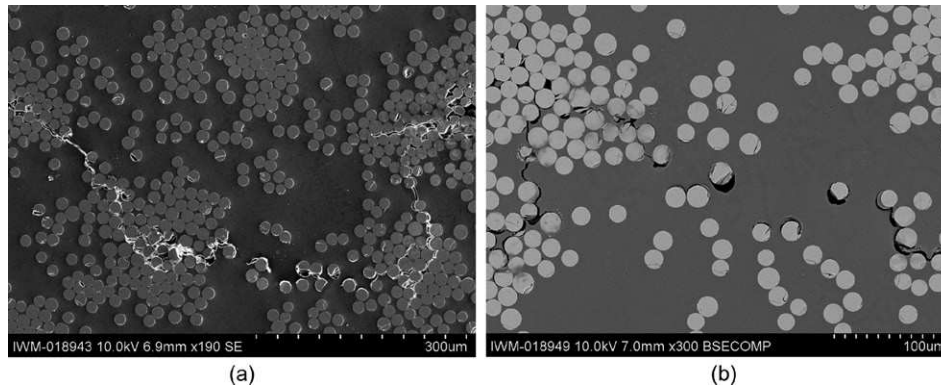
Figure 3.10 SEM micrographs of the cross section behind the visual crack front: forward running failure in the interfaces, mainly in the fiber-rich areas

To investigate the fracture initiation and the actual root cause of the overall fracture behavior, the material's microstructure is analyzed in sections directly behind the macroscopically detectable crack front by means of cross-sectional SEM micrographs, which are shown in Figure 3.10. The fracture is initiated at multiple sites within the highly packed fiber bundles, as shown in Figure 3.10(a). Subsequently, several microcracks merge to a macroscopic crack. The paths of the merging microcracks are rarely formed by the shortest connection between two initiated cracks and commonly follow areas in which high amounts of fibers are present. This behavior can be explained by looking at Figure 3.10(b). Here, it is clearly visible that the crack follows the fiber–matrix interfaces or at least interface-near paths. Before separated cracks in neighboring fiber bundles merge, the interfaces of fibers between those two bundles fail, causing the crack to propagate from interface to interface to interface. Once a crack path is predefined by a sequence of failed interfaces the polymer in-between starts to fail as well. This observation supports the assumption that the fiber–matrix interfaces drive the fracture and are responsible for the fracture surface being very rough, a consequence that leads to

Three different materials are investigated in this chapter. Glass fiber (GF) and carbon fiber (CF) sheet molding compounds with fiber weight fractions of 41% and 51%, respectively, and a polypropylene (PP) long fiber reinforced thermoplastic (LFT) with a fiber weight fraction of 30% are used for the fiber orientation analysis. The GF SMC material and GF LFT material with 10, 20, and 30 wt% are used for the investigation of fiber volume content volumetric images. Finally, the fiber curvature of GF SMC and GF LFT is evaluated for comparison.

3.3.2 Statistics

Orientation Statistics

Fiber orientation functions are probabilistic functions describing the orientation distribution [13]. There are always two redundant orientations in two dimensions and in three-dimensional space as well, taking the symmetry of the sphere into account (cf. Figure 3.15). This leads to

$$\psi(n) = \psi(-n) \tag{3.2}$$

Moreover, the integral over all orientations of the upper half of a unit sphere results in

$$\oint \psi(n)\mathrm{d}n = 1. \tag{3.3}$$
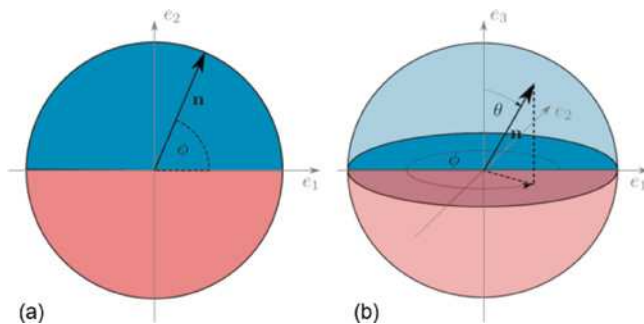

Figure 3.15 Definition of angles for orientation in two (a) and three (b) dimensions. Redundant orientations are depicted in red and blue

Fiber orientation histograms provide a way to build discrete fiber orientation distributions. Figure 3.16 shows an orientation histogram using a polar plot, where the size and color of the data points represent the volume percentage of fibers ori-

ented in a certain direction. A partitioning tool developed by Leopardi [14] is used for discretizing the half sphere. It subdivides the unit sphere into rectangular patches of equal area, rendering an additional weighting function superfluous. These statistics are often used in two-step homogenization approaches for mechanical models [15].
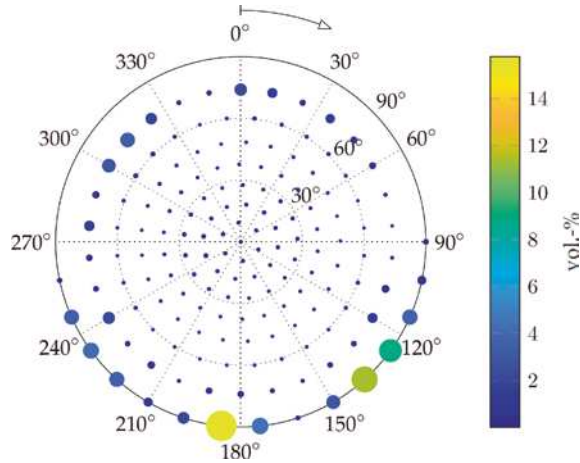
Figure 3.16 Fiber orientation histogram plotted as a polar figure. The size and color of the data points depict the fiber volume fraction oriented in a certain direction

Fiber orientation tensors, introduced by Advani and Tucker [13], offer a very compact way to store fiber orientation data. The orientation tensor of second order can be computed from the orientation distribution functions by

$$N_{ij} = \oint n_i n_j \psi\,(\boldsymbol{n})\ d\boldsymbol{n} \tag{3.4}$$

and the orientation tensor of fourth order by

$$\mathbb{N}_{ijkl} = \oint n_i n_j n_k n_l \psi\,(\boldsymbol{n})\ d\boldsymbol{n}. \tag{3.5}$$

Because orientation analysis from CT data usually results in discrete local orientations in each fiber point, the empirical orientation tensor can be calculated from N fibers by

$$N\,(x) = \frac{1}{N} \sum_{\alpha=1}^{N} \boldsymbol{n}_\alpha \otimes \boldsymbol{n}_\alpha \tag{3.6}$$

for the orientation tensor of second order and

$$\mathbb{N}(x) = \frac{1}{N} \sum_{\alpha=1}^{N} \boldsymbol{n}_\alpha \otimes \boldsymbol{n}_\alpha \otimes \boldsymbol{n}_\alpha \otimes \boldsymbol{n}_\alpha \qquad (3.7)$$

for the fourth-order tensor.

Fiber Length Statistics

Fiber length distributions can be represented in discrete form, where fibers of similar length are clustered into M bins $b_1...b_M$, where each b_i contains the number of fibers within a certain range $l_{i,l} \le l \le l_{i,u}$. The discrete length distribution can be easily evaluated from measured data. Nevertheless, for use with mechanical models, it is beneficial to derive a continuous fiber length distribution function $f_l(L)$. This can be done by curve fitting and the constraint:

$$\int_0^\infty f_l(L)\, \mathrm{d}L = 1. \qquad (3.8)$$

A commonly used model for the fiber length distribution in fiber reinforced polymers is the two-parameter Weibull distribution [15] shown in Figure 3.17.
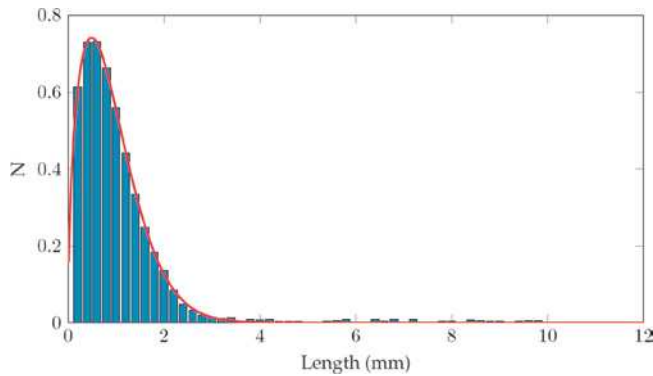
Figure 3.17 Fiber length distribution with respect to the two-parameter Weibull statistic. Blue: discrete data, red: continuous length distribution function

3.3.3 Image Processing

Basic image filters frequently used in fiber orientation analysis are introduced in this section.

Most image operators can be represented by a filter mask, which is convolved [16] with the initial image I:

$$I'(x,y,z) = \sum_{x'=-L}^{L} \sum_{y'=-M}^{M} \sum_{z'=-N}^{N} h(x',y',z')I(x-x',y-y',z-z') \qquad (3.9)$$

where $I'(x,y,z)$ is the filtered image and $h(x',y',z')$ is a filter mask with size $(2L+1) \times (2M+1) \times (2N+1)$. One of the most common image filters is the Gaussian blur. It is derived from the Gaussian function

$$G(x) = \frac{1}{\sigma\sqrt{2\pi}} e^{-\frac{x^2+y^2}{2\sigma^2}}. \qquad (3.10)$$

In the two-dimensional case, the Gaussian blur kernel with $\sigma = 1$ can be expressed by the filter mask

$$G = \frac{1}{273} \begin{bmatrix} 1 & 4 & 7 & 4 & 1 \\ 4 & 16 & 26 & 16 & 4 \\ 7 & 26 & 41 & 26 & 7 \\ 4 & 16 & 26 & 16 & 4 \\ 1 & 4 & 7 & 4 & 1 \end{bmatrix} \qquad (3.11)$$

where division by 273 ensures that the filter is normalized to one [17]. The numerical partial derivatives D_x and D_y can be calculated by convolving the initial image I with the filter mask

$$D_x = \frac{1}{2}[1 \;\; 0 \;\; -1]; \; D_y = \frac{1}{2}\begin{bmatrix} 1 \\ 0 \\ -1 \end{bmatrix} \qquad (3.12)$$

in a two-dimensional image. Consequently, the image gradient reads

$$\text{grad}(I(\mathbf{x})) = \nabla(I(\mathbf{x})) = \begin{bmatrix} \dfrac{\partial I(\mathbf{x})}{\partial x} \\ \dfrac{\partial I(\mathbf{x})}{\partial y} \end{bmatrix} = \begin{bmatrix} D_x \\ D_y \end{bmatrix}. \qquad (3.13)$$

For reasons of efficiency, most of these filters are implemented as recursive filters in practice. The Insight Segmentation and Registration Toolkit (ITK) [17] is used for the implementation of the software presented in this chapter. It provides a recursive implementation of the Gaussian filter and the derivative.

4.2.2 Rheological Measurements and Models

In this section, the newly developed rheological in-line tool is presented and characterization experiments with three different SMCs are performed. Based on these experiments, the compressibility of one SMC class is proven and considered in the rheological models. After determining the material parameters for the different SMCs, a correlation between the parameters and the material composition is developed.

Rheological Tool and Experimental Set-Up

The new rheological tool design is based on the plane strain in-line rheometer (cf. section on Rheological Characterization of SMC). To counteract the disadvantages described earlier, this tool must have a long flow length, a high strain rate range, and a locally high pressure resolution along the flow. Such a tool with a rectangular cavity of 800 mm × 250 mm was designed at the Fraunhofer Institute for Chemical Technology (ICT), in Pfinztal, in which samples with a final thickness between 1 mm and 5 mm can be produced. To measure the pressure over the flow length, seven pressure sensors are integrated along the flow direction (see Figure 4.2). Due to the long possible flow length, different flow behaviors can be observed by varying the initial charge coverage between 20% and 80%. To log the pressure distribution from the pressure sensors simultaneously with the press data (e.g., current press force and the position of the moving mold side), both systems are linked to one recording system. Since the rheological tool is on an industrial scale, the experiments were performed at the Fraunhofer ICT on two industrial hydraulic presses from Dieffenbacher (COMPRESS PLUS DCP-G 3600/3200 AS and Dieffenbacher DYL 630/500).
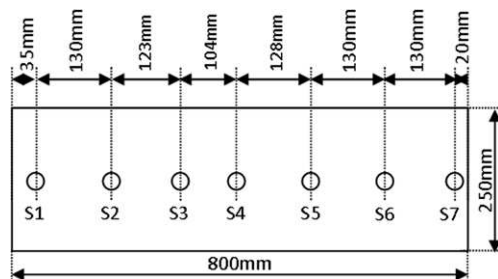
Figure 4.2   Dimensions of the new in-line rheometer and the position of the seven pressure sensors [32]

Three different SMC formulations have been investigated. The first one is an unsaturated polyester (UP)-based low-density (LD) Class-A SMC that was developed for exterior automotive parts by the Fraunhofer ICT [33]. To reduce the density, micro hollow glass spheres were added as part of the filler. The composition of the resin is given in Table 4.1. The second SMC is a semi-structural SMC, which has more

fibers and no fillers. A vinyl ester (VE) resin is used for this formulation (for composition, see Table 4.2). The third formulation is a semi-structural SMC with carbon fibers. Due to the co-molding process with local unidirectional reinforcements (cf. Section 2.2), the B-stage unsaturated polyester polyurethane hybrid (UPPH) resin is used (for composition, see Table 4.3). All these SMC formulations use chopped fibers with a length of 1 inch (approx. 25 mm). The fiber fractions and the fibers used are given in Table 4.4.

In this context, the term "semi-structural" indicates material properties of fiber-reinforced polymers between those of surface parts as Class-A SMC and continuous reinforced polymers.

Table 4.1 Composition of the Paste of the LD Class–A SMC [32, 33]

Component	Trade name	Quantity
UP resin	Palapreg Premium G22–01 LE	100 parts
Adherent and flow aids	BYK W9010	3 parts
Styrol	–	7 parts
Peroxide	Palapreg Premium G21–01LE Cure	1 part
L&V 50%MgO	Luvatol® MK35	2.77 parts
Filler: calcium carbonate	Omya Millicarb	105 parts
Filler: micro hollow glass spheres	3M VS5500	28 parts

Table 4.2 Composition of the Paste of the Semi–Structural VE SMC [34]

Component	Trade name	Quantity
VE resin	Atlac XP810X	100 parts
Adherent and flow aids	BYK 9085	2 parts
Peroxide	Trigonox 117	1 part
L&V 50%MgO	Luvatol EK 100KM	4.2 parts

Table 4.3 Composition of the Paste of the Semi–Structural UPPH Carbon Fiber SMC [34]

Component	Trade name	Quantity
UPPH resin	Daron ZW 14142	100 parts
Adherent and flow aids	BYK 9085	2 parts
Impregnation aid	BYK 9076	3 parts
Deaeration aid	BYK A–530	0.5 parts
Inhibitor	pBQ	0.03 parts
Peroxide	Trigonox 117	1 part
Isocyanate	Lupranat M20R	24.2 parts

Table 4.4   Fiber Type, Fiber Volume, and Length of the SMC Formulations [34]

	LD Class-A SMC	VE SMC	UPPH C-SMC
Fiber type	Glass fiber	Glass fiber	Carbon fiber
Trade name	JM MultiStar® 272	JM MultiStar® 272	Zoltek PX 35
Fiber roving bundles	4800 tex/12K	4800 tex/12K	2700tex/50K
Fiber diameter	13.5 μm	13.5 μm	7.2 μm
Fiber length	25 mm (1 inch)	25 mm (1 inch)	25 mm (1 inch)
Fiber fraction	38 wt% (20 vol%)	41 wt% (22.7 vol%)	55 wt% (42 vol%)

Rheological Measurements of Different SMC Formulations

Slightly different process settings and initial charge (IC) coverings are necessary due to the different resin systems used for the SMC formulations. These are given in Table 4.5. All materials are molded with a constant closing speed of 1 mm s^{-1} for direct comparison. Furthermore, tests with other constant closing speeds and strain rates are performed to characterize the different SMC formulations. Here, the nominal strain rate D is defined as the ratio of the current closing speed $\dot{h}(t)$ and the gap height $h(t)$:

$$D(t) = \frac{|\dot{h}(t)|}{h(t)} \tag{4.7}$$

**Table 4.5**   Process Settings for the Different Material Molding Trials

	LD Class-A SMC	VE SMC	UPPH C-SMC
Tool temperature	Upper: 150 °C Lower: 160 °C	Upper: 150 °C Lower: 160 °C	Upper: 140 °C Lower: 145 °C
Max press pressure	2000 kN	1600 kN	3000 kN
IC coverage	36.25% (290 mm)	20% (160 mm)	20% (160 mm)
IC av. height	9.0 mm (4 layer)	10.1 mm (8 layer)	18.0 mm (16 layer)
IC av. weight	890 g	648 g	970 g
Part av. height	3.2 mm	2.2 mm	3.2 mm

Three exemplary pressure distributions of the different material compositions for a constant closing speed of 1 mm s^{-1} are given in Figure 4.3, Figure 4.4, and Figure 4.5. These diagrams are plotted over the relative gap height, defined as the difference between the current gap height $h(t)$ and the final gap height h_f. This makes it easier to compare the different process settings. When comparing these pressure distributions, the same pattern in different characteristic features can be observed. At the beginning of the molding process, the sensors covered by the initial charge show an increase up to a threshold. During this short phase, the mate-

rial is compressed and trapped air is released. After this transversal compression, the flow of SMC starts. During this flow phase, the pressure is increasing continuously due to the increased friction stress. For the semi-structural VE-SMC, this increase is lower, since the strain rate is increasing and therefore the rheological stress is decreasing (cf. Eq. (4.1) and (4.2)). This already implies a higher extensional viscosity compared to the other material formulations. For the two semi-structural SMC formulations, the pressure of sensor 1 decreases during this phase. This is due to a small defect of the short pegboard, which causes some material to flow through the gap between the tool sides. After the material in this gap is cured, the pressure is restored. Just before the final plate thickness is reached, the maximum pressure can be observed. This is the switching point, where the maximum compression force is reached and the press switches to the pressure controlled closing speed.
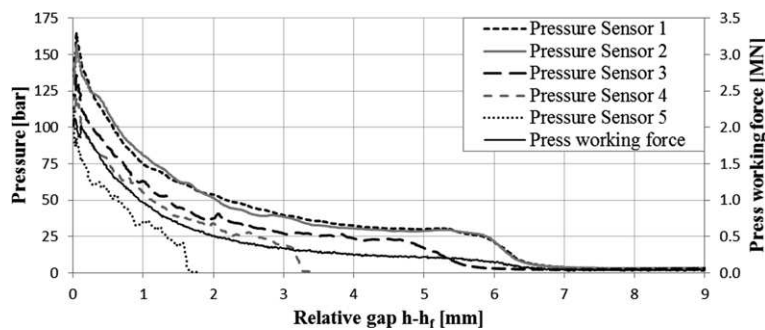
Figure 4.3 Pressure distribution for the LD Class-A SMC for a closing speed of 1 mm s^{-1} [32]
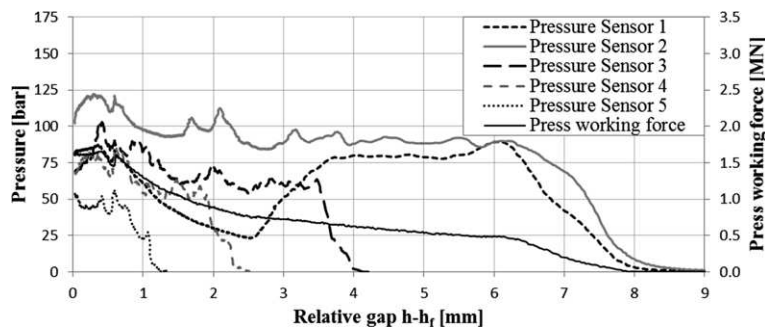
Figure 4.4 Pressure distribution for the semi–structural VE SMC for a closing speed of 1 mm s^{-1} [32]

The model is validated by means of tensile tests on unsaturated polyester polyurethane hybrid and epoxy resin systems with varying glass fiber contents.

4.6.2 Continuum Mechanical Model

Microstructure of SMC Composites

Here, the SMC composite is treated as a two-phase composite consisting of a thermoset matrix phase ω_M and glass fibers ω_F. The matrix is characterized linear elastically by an isotropic matrix stiffness tensor $\mathbb{C}_M$ and the corresponding volume fraction c_M. All fibers are modeled linear elastic with an isotropic stiffness $\mathbb{C}_F$. Due to the low shear rates in the compression molding process, fiber bending and breakage are neglected.

As shown, e.g., by Jendli et al. [121], fiber breakage is the least important damage phenomenon in SMC composites. In-situ experiments showed that fibers usually break only due to macroscopic crack propagation within the specimen. The fibers are modeled as straight ellipsoids with a uniform aspect ratio a_v. The unit vector $\boldsymbol{n}$ describes the orientation of a fiber. The fiber volume fraction $c_F = 1 - c_M$.
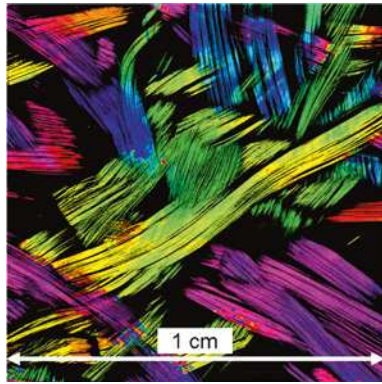
Figure 4.31 Micro-computed tomography scan of an SMC composite microstructure (UPPH resin) [135]. Colors indicate fiber orientation in the corresponding voxel

Figure 4.31 depicts a sliced micro-computed tomography (μCT) scan of an SMC composite. The colors indicate the fiber orientation in each voxel. The fiber filaments for the SMC manufacturing process are utilized in bundles of thousands of filaments. During the impregnation and compression molding, the fiber filaments partially disperse. Motaghi and Hrymak [136] characterized the tow distortion in SMC composites. The remaining short-range order of fiber orientation and volume fraction is neglected, since only the one-point statistic of the microstructure is considered. A scale separation between the microscale dimensions (e.g., fiber length:

25.4 mm or the microstructure in Figure 4.31) and typical component dimensions (2–4 mm thickness and in-plane dimensions of up to two meters) is not admissible. Traditional homogenization schemes are based on the assumption of a scale separation and the existence of a representative volume element. The application of mean-field homogenization schemes in SMC is state of the art and has proven to lead to satisfying results in many two-scale structural simulations.

The fiber orientation distribution function $f(\boldsymbol{n})$ (FODF) specifies the volume fraction $\mathrm{d}v/v$ of fibers with orientation $\boldsymbol{n}$ relative to the total fiber volume (see, e.g., [89]):

$$\frac{\mathrm{d}v}{v}(\boldsymbol{n}) = f(\boldsymbol{n})\mathrm{d}S. \tag{4.56}$$

Here, $\mathrm{d}S$ is the surface element on the unit sphere $S := \{\boldsymbol{n} \in \mathbb{R}^3 : \|\boldsymbol{n}\| = 1\}$. The FODF is non-negative, normalized, and symmetric:

$$f(\boldsymbol{n}) \geq 0, \ \textstyle\int_S f(\boldsymbol{n})\mathrm{d}S, \ f(\boldsymbol{n}) = f(-\boldsymbol{n}), \ \forall \boldsymbol{n} \in S. \tag{4.57}$$

The FODF represents a one-point correlation function of the microstructure and is, therefore, the most simple statistical description of the fiber-dominated microstructure. A distributional representation of $f(\boldsymbol{n})$ with K vectors $\boldsymbol{n}_\beta$ and corresponding weights $c(\boldsymbol{n}_\beta)$ is given by an empirical definition of the fiber orientation distribution with the Dirac delta function $\delta(\boldsymbol{n}, \boldsymbol{n}_\beta)$:

$$f(\boldsymbol{n}) = \textstyle\sum_{\beta=1}^{K} c(\boldsymbol{n}_\beta)\delta(\boldsymbol{n}, \boldsymbol{n}_\beta). \tag{4.58}$$

The weights $c(\boldsymbol{n}_\beta)$ can be interpreted as the volume fraction of fibers oriented in direction $\boldsymbol{n}_\beta$ with respect to the total volume fraction c_F. The relations in Eq. (4.57) imply the following properties of $c(\boldsymbol{n}_\beta)$:

$$c(\boldsymbol{n}_\beta) \geq 0, \ \textstyle\sum_{\beta=1}^{K} c(\boldsymbol{n}_\beta) = 1, \ c(\boldsymbol{n}_\beta) = c(-\boldsymbol{n}_\beta), \ \forall \, \beta = 1 \ldots K. \tag{4.59}$$

We further introduce the abbreviation $c_\beta = c(\boldsymbol{n}_\beta)$. A uniform empirical fiber orientation distribution can be expressed by uniform weights $c_\beta = 1/K$ and a (planar) isotropic distribution of $\boldsymbol{n}_\beta$ on the unit circle or sphere, respectively. The consideration of more directions $\boldsymbol{n}_\beta$ allows for a better discretization of a continuous fiber orientation distribution.

Mori–Tanaka Type Homogenization of Linear Elastic Behavior

The following section describes the estimation of the effective (macroscopic) stiffness tensor and stress localization tensors based on the Mori–Tanaka estimate

[84]. The relation between the macroscopic stress $\overline{\boldsymbol{\sigma}}$ and strain $\overline{\boldsymbol{\varepsilon}}$ is given by the actual macroscopic stiffness tensor $\overline{\mathbb{C}}$ is

$$\overline{\boldsymbol{\sigma}} = \overline{\mathbb{C}}\left[\overline{\boldsymbol{\varepsilon}}\right].\tag{4.60}$$

The fundamental assumption of the Mori–Tanaka homogenization scheme is that the strain localization in the fibers is calculated from the phase-averaged matrix strain $\boldsymbol{\varepsilon}_M$ instead of the macroscopic strain, by the application of the classical Eshelby [83] relation. The Mori–Tanaka stiffness thus reads (see, e.g., [137])

$$\overline{\mathbb{C}} = \mathbb{C}_M + c_F \left(c_M \left\langle \left(\mathbb{P}_0 + (\mathbb{C}_F - \mathbb{C}_M)^{-1} \right)^{-1} \right\rangle_F + c_F \left(\mathbb{C}_F - \mathbb{C}_M \right)^{-1} \right)^{-1}.\tag{4.61}$$

An explicit expression of the symmetric polarization tensor $\mathbb{P}_0 = \mathbb{E}_0 \mathbb{C}_M^{-1} \mathbb{P}_0$ [138], where $\mathbb{E}_0$ is the Eshelby tensor. An analytical, continuous formulation (following Eq. (4.56)) of the orientation average of an arbitrary reference tensor $\mathbb{A}$ over all fibers $\langle \mathbb{A} \rangle_F$ in terms of second-and fourth-order orientation tensors was proposed by Advani and Tucker III [115]. A reformulation of the fiber orientation average based on the Rayleigh product and the empirical formulation (see Eq. (4.58)) leads to

$$\langle \mathbb{A} \rangle_F = \sum_{\beta=1}^{K} c_\beta \boldsymbol{Q}\left(\boldsymbol{n}_\beta\right) \star \mathbb{A}_0, \boldsymbol{Q}\left(\boldsymbol{n}_\beta\right) \in Orth,\tag{4.62}$$

where $\mathbb{A}_0 = \mathbb{A}(\boldsymbol{e}_1)$ is an arbitrary tensor in the reference orientation $\boldsymbol{e}_1$ and $\boldsymbol{Q}(\boldsymbol{n}_\beta)$ is defined as the rotation (i.e., a proper orthogonal tensor) between the reference orientation $\boldsymbol{e}_1$ and $\boldsymbol{n}_\beta$. The phase-averaged matrix and fiber stresses $\boldsymbol{\sigma}_M$ and $\boldsymbol{\sigma}_F$ can be expressed as follows with their corresponding stress localization tensors $\mathbb{B}_M^{MT}$ and $\mathbb{B}_F^{MT}$ of the Mori–Tanaka homogenization:

$$\boldsymbol{\sigma}_M = \mathbb{B}_M^{MT}\left[\overline{\boldsymbol{\sigma}}\right] \text{ and } \boldsymbol{\sigma}_F = \mathbb{B}_F^{MT}\left[\overline{\boldsymbol{\sigma}}\right].\tag{4.63}$$

The localization tensors are determined by

$$\mathbb{B}_M^{MT}\left[\overline{\boldsymbol{\sigma}}\right] = \left(c_M \mathbb{I}^s + c_F \left\langle \mathbb{B}_{F0}^{SIP} \right\rangle_F\right)^{-1}, \mathbb{B}_F^{MT} = \left\langle \mathbb{B}_{F0}^{SIP} \right\rangle_F \mathbb{B}_M^{MT}.\tag{4.64}$$

The fiber stress localization tensor in the single inclusion problem (SIP) in the reference orientation $\mathbb{B}_{F0}^{SIP}$ is given by

$$\mathbb{B}_{F0}^{SIP} = \left(\mathbb{I}^s + \mathbb{C}_M \left(\mathbb{I}^s - \mathbb{P}_0 \mathbb{C}_M \right) \left(\mathbb{C}_F^{-1} - \mathbb{C}_M^{-1} \right) \right)^{-1}.\tag{4.65}$$

Duschlbauer et al. [139] outlined the calculation of the directionally-dependent fiber stress:

$$\sigma_{\mathrm{F}}^{\angle}\left(\boldsymbol{n}_{\beta}\right) = \mathbb{B}_{\mathrm{F}}^{\mathrm{SIP}\angle}\left(\boldsymbol{n}_{\beta}\right) \mathbb{B}_{\mathrm{M}}^{\mathrm{MT}}\left[\overline{\sigma}\right]. \tag{4.66}$$

A rotation of $\mathbb{B}_{\mathrm{F0}}^{\mathrm{SIP}}$ such that the transversely isotropic axis points in direction $\boldsymbol{n}_{\beta}$ leads to $\mathbb{B}_{\mathrm{F}}^{\mathrm{SIP}\angle}$:

$$\mathbb{B}_{\mathrm{F}}^{\mathrm{SIP}\angle}\left(\boldsymbol{n}_{\beta}\right) = \boldsymbol{Q}\left(\boldsymbol{n}_{\beta}\right) \star \mathbb{B}_{\mathrm{F0}}^{\mathrm{SIP}}, \ \boldsymbol{Q} \in Orth. \tag{4.67}$$

Figure 4.32 visualizes the directionally-dependent fiber principal stresses for a horizontal, uniaxial tensile load and a planar, isotropic fiber orientation distribution. Arrows indicate the principal stress direction. In all fiber directions, the stress state is almost planar. The fibers in the tensile direction experience the highest principal stress. Compressive stresses in fibers perpendicular to the tensile direction arise because the fibers contract less than the matrix in the lateral direction. If the composite strength is loaded on the material combinations considered here, the principal stress in the fiber never reaches the 90% confidence level of the fiber strength. Inter alia, this supports the assumption of negligible fiber breakage.
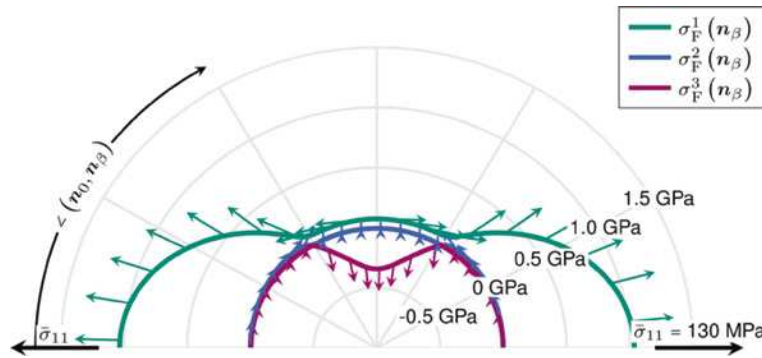
Figure 4.32 Fiber principal stresses $\sigma_{\mathrm{F}}^{\alpha}$ as a function of the fiber orientations $\boldsymbol{n}_{\beta}$ under macroscopic uniaxial tension in the horizontal direction ($\overline{\boldsymbol{\sigma}} = \overline{\sigma}_{11} \boldsymbol{e}_1 \otimes \boldsymbol{e}_1$). Arrows indicate the principal stress direction

Modeling the Matrix Damage

The damage behavior of the matrix is modeled by an isotropic degradation of the initial matrix stiffness $\mathbb{C}_{\mathrm{M}}^0$, which leads to the following relation for the isotropic matrix stiffness $\mathbb{C}_{\mathrm{M}}$:

$$\mathbb{C}_{\mathrm{M}} = (1 - d_{\mathrm{M}}) \, \mathbb{C}_{\mathrm{M}}^0. \tag{4.68}$$

The damage variable d_{M} is determined as a function of the maximum value of the phase-averaged principal matrix stresses in the prior loading history of the matrix:

$$d_{\mathrm{M}} = d_{\mathrm{M}} \left(\max_{\tau \in [0,t]} \left(\max_{\alpha=1,2,3} \sigma_{\mathrm{M}}^{\alpha} \right) \right). \tag{4.69}$$

Since the thermoset matrix is considered a brittle material, a maximum stress criterion was applied, assuming that the material failure is governed by the highest principal stress. The outer max-function ensures that d_{M} is monotonically increasing, i.e., that there is no healing, even for load histories that include unloading.

Modeling the Fiber–Matrix Interface Debonding

Fibers are considered cylindrical with a large aspect ratio, for which the debonding of head surfaces (Figure 4.33) was ignored. In doing so, the influence of head-surface debonding on the effective stiffness is assumed to be small. Additionally, the coupling of debonding of head surfaces with other damage phenomena, such as crack propagation into the lateral surface or matrix, was ignored.
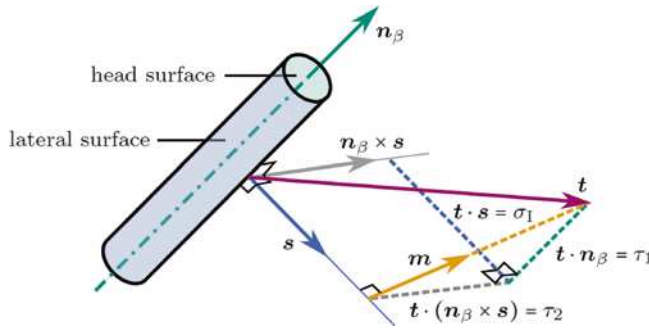
Figure 4.33 Single fiber with orientation $\boldsymbol{n}_\beta$, an outer normal vector s, and a tangential vector $\boldsymbol{m}$ on its lateral shell surface

Interface damage was assumed to be governed solely by the stress on the lateral surface of the interface only. Cauchy's Lemma gives the interface stress vector $\boldsymbol{t}$ as a function of the fiber orientation $\boldsymbol{n}_\beta$ and the lateral surface normal $\boldsymbol{s}$ (see Figure 4.33) if the phase-averaged stress tensor $\boldsymbol{\sigma}_{\mathrm{F}}^{\angle}(\boldsymbol{n}_\beta)$ of a fiber with orientation $\boldsymbol{n}_\beta$ is known:

$$\boldsymbol{t}(\boldsymbol{n}_\beta, \boldsymbol{s}) = \boldsymbol{\sigma}_{\mathrm{F}}^{\angle}(\boldsymbol{n}_\beta) \, [\boldsymbol{s}]. \tag{4.70}$$

The interface stress vector is decomposed into its normal σ_{I} and shear τ_{I} components, thus,

$$\boldsymbol{t}(\boldsymbol{n}_\beta, \boldsymbol{s}) = \sigma_{\mathrm{I}}(\boldsymbol{n}_\beta, \boldsymbol{s})\boldsymbol{s} + \tau_{\mathrm{I}}(\boldsymbol{n}_\beta, \boldsymbol{s})\boldsymbol{m} \text{ and } \boldsymbol{s} \perp \boldsymbol{n}_\beta, \boldsymbol{m} \perp \boldsymbol{s}, \ \tau_{\mathrm{I}}(\boldsymbol{n}_\beta, \boldsymbol{s}) \geq 0, \tag{4.71}$$